Additive-induced Crystallization of Inorganic Perovskite Films for Efficient Solar Cells

Huijie Zhang[1], Jing Li[1], Zhen Huang[1], Wenkang Wang[1], Jinhua Li,
Duofa Wang[1,2,3] *, and Tianjin Zhang[1,2,3*]

[1] Hubei Collaborat ive Innovation Center for Advanced Organic Chemical Materials, Hubei University, Wuhan 430062, People's Republic of China
[2] Key Laboratory for the Green Preparation and Application of Functional Materials, Ministry of Education, Hubei University, Wuhan 430062, People's Republic of China
[3] School of Material Science and Engineering, Hubei University, Wuhan 430062, People's Republic of China
[*]E-mail: duofawang@hotmail.com, zhangtj@hubu.edu.cn

In recent years, hybrid perovskite solar cells (PSCs) have received extensive attention because of their high power conversion efficiency (PCE), yet their thermal stability is still not ideal. Meanwhile, all-inorganic PSCs have excellent thermal stability, but their device efficiency is relatively low. Here we report the use of non-toxic additive-induced crystallization to improve film quality to enhance the efficiency of all-inorganic PSCs. High-quality perovskite films with full surface coverage and uniform grain structure were prepared. Kinetic analysis of the crystallization process showed that the non-toxic additive increased the supersaturation of the perovskite precursor and induced rapid nucleation and crystallization. The optical band gap of the perovskite films was tuned by adjusting iodide content. $CsPbBrI_2$ with an appropriate bandgap was used as the light-absorbing material in PSCs that displayed high thermal stability. By optimizing the preparation process, an all-inorganic PSC with a planar structure delivered a PCE of 5.6%. The entire device fabrication process was performed in the ambient environment without humidity control. Thus, we developed a simple, controllable, and versatile approach to produce high-quality inorganic perovskite films for use in high-performance photovoltaic devices.

1. INTRODUCTION

Hybrid organic–inorganic perovskite solar cells (PSCs) are attracting increasing interest because of their excellent photovoltaic (PV) performance and facile, cheap fabrication, which make

them promising to provide renewable clean energy for human society in the future[1-8]. In the past few years, most research in this field has focused on how to improve the power conversion efficiencies (PCEs) of PSCs; the certified highest PCE achieved to date is 22.1%[9, 10]. Although PCEs have been greatly improved through the optimization of fabrication techniques, hybrid perovskite absorber layers, such as methylammonium lead triiodide ($MAPbI_3$) and formamidinium lead triiodide ($FAPbI_3$), are susceptible to compositional degradation induced by heat and humidity[11], which is a major technical hurdle to commercialization. To circumvent this problem, cesium lead halide materials have been used as substitutional absorber layers in PSCs. The stability of cesium lead halide PSCs is superior to those with $MAPbI_3$ and $FAPbI_3$ because they are less hygroscopic than devices containing the methyl ammonium cation and also display higher thermal stability[12-15]. It has been reported that cesium lead iodide ($CsPbI_3$) has a suitable optical band gap (1.73 eV) for use as the active layer of PSCs. Unfortunately, the black perovskite phase of $CsPbI_3$ is unstable in ambient atmosphere and rapidly converts to the non-perovskite yellow phase[16, 17]. Recently, by substituting the $CsPbI_3$ lattice with a certain percentage of bromine, its bandgap was tuned between about 1.90 and 2.13 eV, which improved its optical and thermal stability compared with those of $MAPbI_3$ and enhanced its structural phase stability relative to that of undoped $CsPbI_3$[18]. Compared with hybrid PSCs, the primary problem of all-inorganic PSCs is still to improve their PCE[19-22].

To obtain favorable device performance, a compact pinhole-free perovskite film is needed to provide high delivery efficiency[23]. However, is difficult to produce homogeneous perovskite films using the conventional one-step spin-coating method; some pinholes tend to form in the films and degrade the performance of the resulting PSCs. The pinholes not only weaken the light absorption ability of the perovskite layer, but also hinder charge transport[24]. In organic–inorganic hybrid PSCs, solvent engineering has been used as a pioneering technique to improve film quality and enhance device efficiency[25-29]. Jeon et al.[25] and Xiao et al.[26] used toluene and chlorobenzene, respectively, as additives in solvent engineering to realize the rapid and reproducible fabrication of high-quality $MAPbI_3$ thin films that were used in PSCs with remarkably improved efficiency. Zhou et al.[28] used a diethyl ether solvent bath to induce efficient extraction of the precursor solvent and achieved ultrasmooth $MAPbI_3$ thin films with good thickness control and large-area uniform deposition capability.

In this paper, we use the solvent engineering method employing the environmentally friendly additive ethyl acetate to remove residual precursors in inorganic perovskite thin film formation to obtain full-coverage perovskite films. Ethyl acetate promotes the nucleation and crystallization processes, improving the morphology and crystallinity of perovskite layers. The nucleation and growth theory is used to understand how the crystallization process is affected by this non-toxic additive. Solvent engineering using ethyl acetate increases the PCE of $CsPbBrI_2$ solar cells from 2.94% to 5.62%. Moreover, the perovskite layer remains thermally stable at 150 °C. These results help to lay the foundation for the commercial application of solar cells in the future.

2. EXPERIMENTAL DETAILS

2.1. Fabrication of CsPbBr$_{3-x}$I$_3$ PSCs

The surface of a fluorine-doped tin oxide (FTO) glass substrate was cleaned by sequential sonication in deionized water, acetone, and isopropyl alcohol for 15 min each, followed by drying under a N$_2$ stream. The samples were treated with UV/ozone for 20 min. A compact TiO$_2$ layer (100 nm thick) was fabricated by spin-coating at 3500 rpm for 30 s from a 0.15 M titanium diisopropoxide bis(acetylacetonate) solution in anhydrous ethanol and annealing at 500 °C for 30 min in air. A CsPbBr$_{3-x}$I$_x$ (1<x<2) film was then prepared by a one-step spin-coating method. First, a 0.72 M inorganic perovskite precursor solution was obtained by dissolving stoichiometric amounts of PbBr$_2$ (Aldrich), PbI$_2$ (Aldrich), and CsI in DMF/DMSO. The precursor solution was spin-coated on a preheated (70 °C) TiO$_2$-coated FTO substrate at 3000 rpm for 30 s and then dried on a hot plate at 100 °C for 5 min. In some cases, ethyl acetate was dripped at certain times during the high-speed spin-coating of the CsPbBrI$_2$ precursor solution instead of heat treatment. The hole transport layer of the devices was then deposited by spin-coating (4000 rpm) a solution of spiro-MeOTAD (Merck, 72.3 mg), 4-*tert*-butylpyridine (28.8 μL), and lithium bis(trifluoromethanesulfonyl)imide (Li-TFSI) solution [17.5 μL; consisting of Li-TSFI (52 mg) in acetonitrile (1 mL, Sigma-Aldrich, 99.8%)] in chlorobenzene (1 mL)[30, 31]. All procedures were carried out in ambient air (relative humidity: 40%–60%). Finally, the devices were completed by deposition of gold (Au) electrodes.

2.2. Characterization

The morphology of the perovskite layers was observed with a field emission scanning electron microscope (FE-SEM, JSM-7100F, JEOL). X-ray diffraction (XRD) was per-formed using a Rigaku D/MAX-3A X-ray diffractometer with Cu Kα radiation (k=0.15406 nm) at a scan rate of 5°/min. The optical spectroscopy of the inorganic perovskite thin films was conducted on a UV–visible–NIR spectrophotometer (UV-3600, JEOL). The photocurrent density–voltage (*J-V*) curves of the assembled CsPbBrI$_2$ PSCs were measured using a Keithley 2400 source meter with simulated AM1.5 sunlight with an output power of 100 mW/cm^2 produced by a solar simulator (Newport 91192).

3. RESULTS AND DISCUSSION

The ethyl acetate (EA) extraction technique used to prepare CsPbBr$_{3-x}$I$_x$ films is compared with the conventional one-step spin-coating method in Fig. 1a. First, a FTO substrate with a deposited TiO$_2$ layer was treated by UV/ozone. Second, a mixture of CsI, PbI$_2$, PbBr$_2$, DMF, and DMSO was spread over the entire surface of the substrate. After a specific spin-coating time (e.g., 10 s), EA was quickly dropped onto the substrate during the high-speed spin-coating; the film then rapidly became brownish black. The role of the non-polar EA is to rapidly lower the solubility of CsPbBrI$_2$ in the mixed solvent, thereby promoting immediate nucleation and crystallization on the substrate. In contrast, in conventional spin-coating, the wet film dried slowly and a shiny gray film was obtained, which needed

to be annealed at 100 °C for 5 min to remove residual solvent and promote further crystallization. The SEM images (Fig. 1b and c) of the surface reveal that the morphology of the perovskite layer is markedly changed by the EA extraction technique. The shiny gray film obtained by conventional spin-coating contained larger discontinuous grains with low coverage on the substrate. Meanwhile, The film grown in the presence of EA was uniform and dense, and fully covered the surface with low surface roughness.
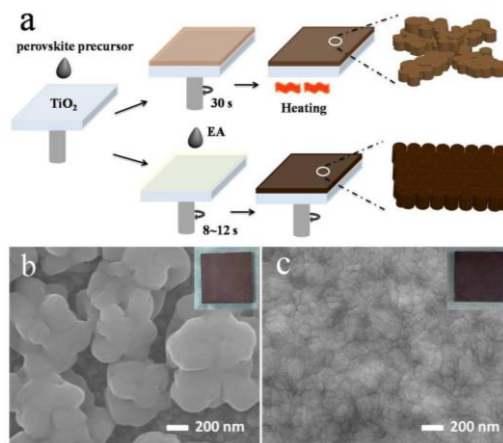
Figure 1. (a) Schematic illustration of the solvent-treatment process and conventional spin-coating process used to fabricate inorganic perovskite films. Conventional spin-coating (top) results in a brown film composed of non-uniform large crystals as a result of slow crystallization. In the solvent-treatment process (bottom), ethyl acetate introduced on top of the wet film during the nucleation process induces fast crystallization of uniform-sized perovskite grains. (b, c) SEM images of $CsPbBrI_2$ perovskite layers formed using conventional spin-coating and ethyl acetate, respectively. Inset are photographs of the corresponding $CsPbBrI_2$ films.

To determine the reasons for the differences between these inorganic perovskite films prepared under different processing conditions, we investigated their crystallization process. In the solution spin-coating method, the nucleation and growth of crystals are driven by the supersaturation ξ, which is defined as[32]

$$\xi = (\rho_s - \rho_e)/\rho_e = (\rho_s/\rho_e) - 1,$$

where ρ_s is the supersaturation concentration and ρ_e is the equilibrium concentration. During conventional spin-coating, the perovskite precursor solutions sequentially reach equilibrium and supersaturation during solvent evaporation, and then begin to nucleate. Adding EA during the high-speed spin-coating process rapidly removed the residual solvent, causing early supersaturation of the solution, resulting in increased ρ_s and ξ and rapid nucleation of perovskite crystals (Fig. 2). According to the thin-film growth theory[32], high ξ leads to a small critical nucleus radius, high nucleation density[27, 33-36], and is favorable for layer growth of perovskite films. This behavior is consistent with the SEM image of a $CsPbBrI_2$ film prepared using the EA extraction technique (Fig. 1c). In contrast, the conventional one-step spin-coating method gave large crystals and aggregations (Fig. 1b), leading to the formation of pinholes in the perovskite films. These results indicate that the nucleation density during spin-coating directly determines the ultimate morphology of perovskite films.

Therefore, raised supersaturation and high nucleation density can help to produce perovskite films with homogeneous morphology.
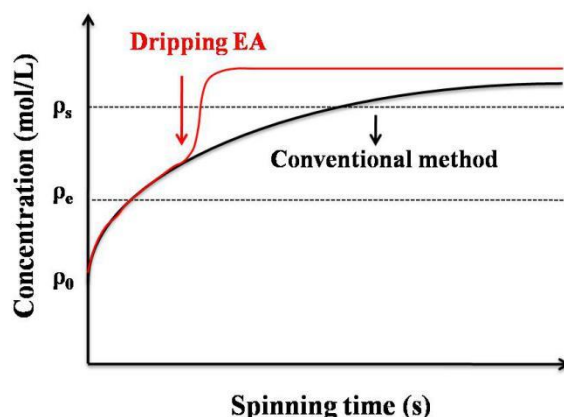
Figure 2. Schematic illustration for nucleation during spin-coating: the relation between perovskite solution concentration and spinning time (ρ_o is concentration of precursor solution, ρ_e is concentration of equilibrium status and ρ_s is concentration of supersaturation).
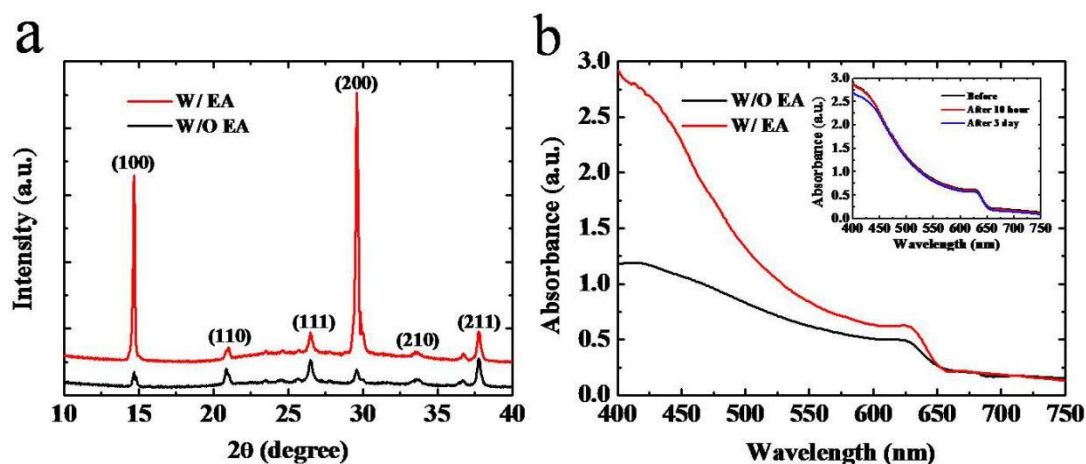
Figure 3. (a) XRD patterns of $CsPbBrI_2$ thin films prepared with or without ethyl acetate. (b) Absorption spectra of $CsPbBrI_2$ thin films. Inset are UV-vis absorption spectra of $CsPbBrI_2$ films fabricated with ethyl acetate and then heated at 150 °C in ambient air for different periods.

XRD analysis (Fig. 3a) revealed that the intensities of the diffraction peaks at 14.67° and 29.54°, assigned to (100) and (200) of the $CsPbBrI_2$ crystal, respectively, increased in the presence of EA, which suggests that EA facilitates the growth of crystals toward the (100) direction and enhances crystallinity. The absorption spectra of the films (Fig. 3b) showed that the film by the traditional method had lower absorbance. The XRD and absorption results support EA drived supersaturation and crystallization model, that EA rapidly lowered the solubility of the perovskite precursor and increased nucleation density, providing a high-quality film with full coverage. The $CsPbBrI_2$ films produced

using EA shows much more superior thermal stability than the organic-inorganic perovskite. The absorption spectrum nearly does not change when the sample was heated at 150℃ for three days in ambient air, as shown in the inset of Fig.3b. Whereas, the hybrid appears decomposition even at room temperature due to the presence of volatile organic cations [18, 21, 22]. Thus, these films meet the requirements for commercial applications; in particular, compositional stability under thermal stress is important for long-term operation of solar cells.
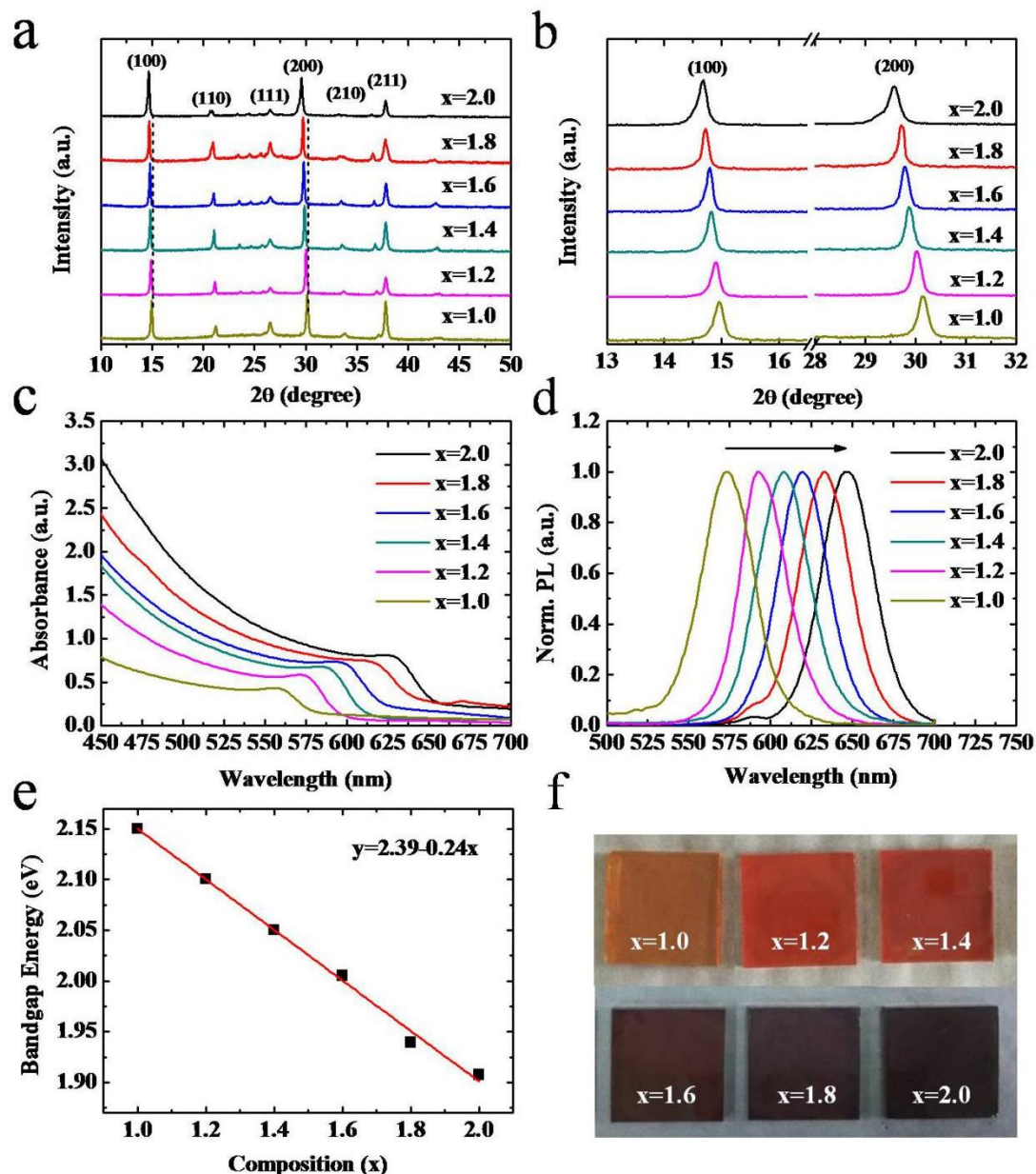
Figure 4. (a) XRD patterns of $CsPbBr_{3-x}I_x$ (x=1–2). (b) Magnified XRD patterns of $CsPbBr_{3-x}I_x$ in the regions near 15° and 30°. (c, d) UV-Vis absorption and photoluminescence spectra of $CsPbBr_{3-x}I_x$/FTO with x=1.0, 1.2, 1.4, 1.6, 1.8, 2.0. (e) Variation of the bandgap energy of the films with increasing I content. (f) Photograph of $CsPbBr_{3-x}I_x$ (x=1–2) thin films under ambient light.

The developed anti-solvent extraction technique is also applicable to $CsPbBr_{3-x}I_x$ (x=1–2) films with different iodine contents. The structure of $CsPbBr_{3-x}I_x$ thin films was examined via XRD; relevant XRD patterns are shown in Fig. 4a. The measured patterns for the $CsPbBr_{3-x}I_x$ films are compatible with literature data for the cubic perovskite structure of $CsPbBr_3$ (PDF#75-0412). In addition, the intensities of the (100) and (200) diffraction peaks are relatively high compared with those reported, suggesting that the processing route used here yields films that are oriented in the (100) direction [18]. When I substitutes Br, lattice expansion occurs because the radius of I^- is larger than that of Br^-. Thus, according to Bragg's law, $n\lambda=2dsin\theta$, there should be a shift of XRD peaks to lower angles (Fig. 4b) as I concentration increases. The optical characterization results (Fig. 4c–e) show that the bandgap of the films can be tuned between about 1.90 and 2.13 eV by varying the contents of I and Br. Notable shifts of the absorption onset and PL peaks to longer wavelengths were observed with increasing I content. The optical bandgaps of $CsPbBr_{3-x}I_x$ were evaluated as a function of (y=2.39−0.24x), as shown in Fig. 4c, indicating that solid solutions of the Br/I mixtures formed throughout this series. A photograph of the perovskite $CsPbBr_{3-x}I_x$ films (Fig. 4f) indicates that smooth, homogeneous perovskite layers formed.
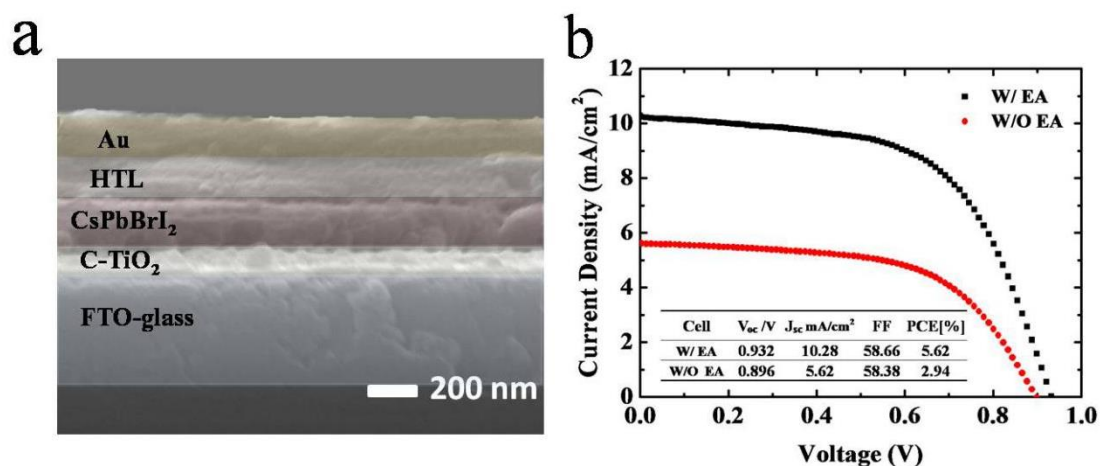
Figure 5. (a) Cross-sectional SEM image of a complete $CsPbBrI_2$ perovskite device with the configuration of $FTO/TiO_2/CsPbBrI_2/Spiro$-OMeTAD/Au. (b) Current density–voltage (*J-V*) characteristics of the solar cell based on the as-prepared inorganic perovskite films under AM 1.5 illumination. Inset are the photovoltaic performance values extracted from the *J–V* curves.

Figure 5 shows the PV performance of a $CsPbBrI_2$ PSC along with a cross-sectional SEM image; the device fabrication process is described in detail of the experimental section. The thickness of each layer was, TiO_2: 112 nm, $CsPbBrI_2$: 200 nm, Spiro-OMeTAD: 160 nm, and Au electrode: 150 nm. Device performance was characterized by *J-V* measurements under simulated AM 1.5 (100 mW/cm^2) solar irradiation in air. As illustrated in Fig. 5b, the optimum device with an EA-treated perovskite layer exhibited outstanding performance, with a high open circuit voltage (V_{OC}) of 0.932 V, short-circuit current density (J_{SC}) of 10.3 mA/cm^2, fill factor (FF) of 0.59, and promising stabilized PCE of 5.62% under standard AM 1.5 conditions. In contrast, the best solar cell prepared using the conventional method possessed a V_{OC} of 0.896 V, J_{SC} of 5.62 mA/cm^2, FF of 0.58, and PCE of 2.94%.

The EA-treated perovskite also shows better film quality and higher PV performance than the literature work with the traditional experimental process[22]. Therefore, we suggest that the improved PCE of the device with an EA-treated perovskite layer is ascribed to the high quality of the perovskite film, with better crystalinity and compactness. As shown in XRD pattern in Fig. 3(a), the EA-treated perovskite exhibits much higher lattice crystalline quality. The defects, such as vacancies and dislocations acting as non-radiative recombination centers must be significantly reduced, which was found to be an important factor affecting the PV performance of the solar cell [24,37]. The excellent compactness of the active layer was supposed to be the second factor contributing to the high PV performance. The density of voids and pinholes in the compact film is greatly decreased, which was reported to benefit enhancing the shunt resistance and thereby increase the light current in the hybrid perovskite solar cell[38]. Moreover, the nearly 100% surface coverage of this film also contributes harvesting light absorption and improving the PV performance[38]. Therefore, we demonstrates that employment of EA is an effective method to improves the perovskite film quality and accordingly boosts cell conversion efficiency.

4. CONCLUSIONS

We reported an anti-solvent extraction technique that is a novel viable approach to fabricate $CsPbBr_{3-x}I_x$ films and their corresponding PV devices with good thermal stability. The inorganic perovskite films derived from this approach exhibited full surface coverage, dense cross-section morphology, uniform grain structure, and promising PV performance. Perovskite films with different optical band gaps can be obtained by adjusting I content. Simultaneously, The film nucleation and growth theory is used to understand how the crystallization process is affected by this anti-solvent extraction technique. Facilitated by the excellent film quality, the $CsPbBrI_2$ materials yielded a PCE of 5.62% for a device with a planar architecture in ambient air. This EA extraction technique represents a simple, controllable, and versatile approach to provide high-quality perovskite films and high-performance all-inorganic PV devices.

References

1. G. Xing, N. Mathews, S. Sun, S. S. Lim, Y. M. Lam, M. Grätzel, S. Mhaisalkar, T. C. Sum, *Science*, 342 (2013) 344-347.
2. H. Zhou, Q. Chen, G. Li, S. Luo, T. Song, H. S. Duan , Z. Hon, J. You, Y. Liu, Y. Yang, *Science*, 345 (2014) 542-546.
3. C. Roldán-Carmona, P. Gratia, I. Zimmermann, G. Grancini, P. Gao, M. Graetzel, M. K. Nazeeruddin, *Energy Environ. Sci.*, 8 (2015) 3550-3556.
4. W. S. Yang, J. H. Noh, N. J. Jeon, Y. C. Kim, S. Ryu, J. Seo and S. I. Seok, *Science*, 348 (2015)

1234-1237.

5. S. D. Stranks and H. J. Snaith, Nat. *Nanotechnol.*, 10 (2015) 391-402.

6. M. Saliba, T. Matsui, J. Y. Seo, K. Domanski, J. P. Correa-Baena, M. K. Nazeeruddin, S. M. Zakeeruddin, W. Tress, A. Abate, A. Hagfeldt and M. Gratzel, *Energy Environ. Sci.*, 9 (2016) 1989-1997.

7. T. Leijtens, G. E. Eperon, N. K. Noel, S. N. Habisreutinger, A. Petrozza, H. J. Snaith, *Adv. Energy Mater.*, 5 (2015) 1500963.

8. N. J. Jeon, J. H. Noh, W. S. Yang, Y. C. Kim, S. Ryu, J. Seo, S. I. Seok, *Nature*, 517 (2015) 476.

9. L. L. Gao, C. X. Li, C. J. Li, G. J. Yang, *J. Mater. Chem. A*, 5 (2017) 1548-1557.

10. NREL, Best Research-Cell Efficiencies, http://www.nrel.gov, accessed: November 2016.

11. B. Conings, J. Drijkoningen, N. Gauquelin, A. Babayigit, J. D'Haen, L. D'Olieslaeger, A. Ethirajan, J. Verbeeck, J. Manca, E. Mosconi, F. De Angelis, H. G. Boyen, *Adv. Energy Mater.*, 5 (2015) 1500477.

12. D. Dong, H. Deng, C. Hu, H. Song, K. Qiao, X. Yang, J. Zhang, F. Cai, J. Tang, and H. Song, *Nanoscale*, 9 (2017) 1567-1574.

13. G. E. Eperon, V. M. Burlakov, P. Docampo, A. Goriely and H. J. Snaith, *Adv. Funct. Mater.*, 24 (2014) 151-157.

14. J. Zhang, X. Yang, H. Deng, K. Qiao, U. Farooq, M. Ishaq, F. Yi, H. Liu, J. Tang, and H. Song, *Nano-Micro Lett.*, 9 (2017) 36-40.

15. M. Kulbak, S. Gupta, N. Kedem, I. Levine, T. Bendikov, G. Hodes, D. Cahen, *J. Phys. Chem. Lett.*, 7 (2015) 167-172.

16. C. K. Moller, *Nature*, 182 (1958) 1436-1436.

17. G. E. Eperon, G. M. Paternò, R. J. Sutton , A. Zampetti, A. A. Haghighirad, F. Cacialli, H. J. Snaith, *J. Mater. Chem. A*, 3 (2015) 19688-19695.

18. R. E. Beal, D. J. Slotcavage, T. Leijtens, A. R. Bowring, R. A. Belisle, W. H. Nguyen, G. F. Burkhard, E. T. Hoke, M. D. McGehee, *J. Phys. Chem. Lett.*, 7 (2016) 746-751.

19. Niezgoda, J. Scott, Benjamin J. Foley, Alexander Z. Chen, and Joshua J. Choi, *ACS Energy Lett.,* 2.5 (2017) 1043-1049.

20. Atourki, L., Vega, E., Mollar, M., Marí, B., Kirou, H., Bouabid, K., & Ihlal, A., *Journal of Alloys and Compounds,* 702 (2017) 404-409.

21. G. E. Eperon, G. M. Paterno, R. J. Sutton, A. Zampetti, A. A. Haghighirad, F. Cacialli and H. J. Snaith, *J. Mater. Chem. A*, 3 (2015) 19688-19695.

22. Y. G. Kim, T. Y. Kim, J. H. Oh, K. S. Choi, Y. J. Kim, S. Y. Kim, *Phys. Chem. Chem. Phys.*, 19 (2017) 6257-6263.

23. G. E. Eperon, V. M. Burlakov, P. Docampo, A. Goriely and H. J. Snaith, *Adv. Funct. Mater.*, 24 (2014) 151-157.

24. H. Gao, C. Bao, F. Li, T. Yu, J. Yang, W. Zhu, X. Zhou, G. Fu and Z. Zou, *ACS Appl. Mater. Interfaces*, 7 (2015) 9110-9117.

25. N. J. Jeon, J. H. Noh, Y. C. Kim, W. S. Yang, S. Ryu, S. I. Seok, *Nat. Mater.*, 13 (2014) 897-903.

26. F. Zhang, J. Song, L. Zhang, F. Niu, Y. Hao, P. Zeng, H. Niu, J. Huang and J. Lian, *J. Mater. Chem. A*, 4 (2016) 8554-8561.

27. M. Xiao, F. Huang, W. Huang, Y. Dkhissi, Y. Zhu, J. Etheridge, A. G. W, U. Bach, Y. B. Cheng, L. Spiccia, *Angew. Chem.*, 126 (2014) 10056-10061.

28. Y. Zhou, M. Yang, W. Wu, A. L. Vasiliev, K. Zhu, N. P. Padture, *J. Mater. Chem. A*, 3 (2015) 8178-8184.

29. M. Yin, F. Xie, H. Chen, X. Yang, F. Ye, E. Bi, Y. Wu, M. Cai, L. Han, *J. Mater. Chem. A*, 4 (2016) 8548-8553.

30. J. Burschka, N. Pellet, S. J. Moon, R. Humphrey-Baker, P. Gao, M. K. Nazeeruddin, M. Grätzel, *Nature*, 499 (2013) 316-319.

31. J. H. Im, I. H. Jang, N. Pellet, M. Grätzel, and N. G. Park, *Nat. Nanotechnol.*, 9 (2014) 927-932.

32. J. A. Venables, Introduction to Surface and Thin Film Processes, Cambridge university press. 2003.
33. G. R. Desiraju, Crystal engineering: A brief overview, *J. Chem. Sci.*, 122 (2010) 667-675.
34. M. Mukhopadhyay, S.V. Dalvi, *J. Chem. Technol. Biotechnol.*, 80 (2005) 445-454.
35. Y. Tidhar, E. Edri, H. Weissman, D. Zohar, G. Hodes, D. Cahen, B. Rybtchinski, S. Kirmayer, *Am. Chem. Soc.*, 136 (2014) 13249-13256.
36. F. Huang, Y. Dkhissi, W. Huang, M. Xiao, I. Benesperi, S. Rubanov, Y. Zhu, X. Lin, L. Jiang, Y. Zhou, A. GrayWeale, J. Etheridge, C. R. McNeill, R. A. Caruso, U. Bach, L. Spiccia and Y. B. Cheng, *Nano Energy*, 10 (2014) 10-18.
37. W. Tress, N. Marinova, O. Inganäs, M. Nazeeruddin, S. M. Zakeeruddin, & M. Graetzel, *Advanced Energy Materials*, 5.3.(2015).
38. C. M. Proctor, & T. Q. Nguyen, *Applied Physics Letters*, 106.8, (2015) 23.